



# Data-driven analysis of hydrogen embrittlement in martensitic steels with interpretable machine learning

Houichi Kitano<sup>\*</sup> , Yuuji Kimura , Akinobu Shibata

National Institute for Materials Science, 1-2-1, Sengen, Tsukuba, Ibaraki 305-0047, Japan

## ARTICLE INFO

### Keywords:

Hydrogen embrittlement  
Martensitic steel  
Machine learning  
Shap (shapley additive explanations)  
Symbolic regression

## ABSTRACT

A data-driven analytical framework integrating machine learning (ML), SHAP (SHapley Additive exPlanations) analysis, and symbolic regression (SR) was developed and applied to quantitatively analyze and interpret hydrogen embrittlement behavior in martensitic steels. Slow strain rate tests (SSRT) were conducted on JIS-SCM440 steels with systematically varied diffusible hydrogen contents, phosphorus contents, and tempering conditions to construct an experimental database. The ML model accurately predicted the notch tensile strength, and SHAP analysis quantitatively evaluated the contributions and interactions of the key factors. The SHAP results were then simplified to extract dominant trends, which were interpreted from a metallurgical perspective to elucidate the characteristic dependencies of hydrogen embrittlement on hydrogen content, phosphorus content, and tempering conditions. Based on these insights, SR was applied to formulate explicit and interpretable equations representing these relationships. The resulting model not only reproduces the characteristic physical behavior associated with hydrogen embrittlement but also establishes a quantitative framework linking data-driven analysis and metallurgical understanding, providing a rational basis for the design and safety assessment of high-strength martensitic steels used in hydrogen infrastructure applications.

## 1. Introduction

In recent years, the utilization of low-cost and high-strength low-alloy steels, particularly martensitic steels, has been strongly desired for hydrogen infrastructure applications to reduce construction costs and accelerate large-scale implementation. However, to achieve the practical use of martensitic steels in hydrogen-related components, the issue of hydrogen embrittlement must be overcome. Hydrogen embrittlement significantly reduces the ductility and load-bearing capacity of steels, leading to sudden fracture, and thus limits the reliability and safety of hydrogen infrastructure systems. Therefore, a comprehensive understanding and control of hydrogen embrittlement behavior in martensitic steels, together with the establishment of design guidelines for improving hydrogen embrittlement resistance, are critically important for the advancement of a hydrogen-based society.

The mechanisms of hydrogen embrittlement have been extensively studied, and several representative models have been proposed, including hydrogen-enhanced decohesion (HEDE) [1–5], hydrogen-enhanced localized plasticity (HELP) [6–10], and hydrogen-enhanced strain-induced vacancies (HESIV) [11–13]. Although these models

differ in detail, they share a common framework: hydrogen promotes fracture by altering the bonding state and deformation behavior inside the material. Accordingly, to understand and control hydrogen embrittlement behavior, it is essential to clarify the relationship among the internal hydrogen content, microstructural state, and the resulting embrittlement response.

In martensitic steels, specific factors influencing hydrogen embrittlement have been investigated in detail. Previous studies have revealed that the major controlling factors are: (1) the diffusible hydrogen content, which directly causes embrittlement; (2) impurity elements, particularly phosphorus, which influence the hydrogen distribution and the intrinsic strength of the material; and (3) the tempering conditions, which determine the microstructural features such as carbide morphology [14–17]. However, most of these studies have focused primarily on qualitative discussions, and therefore, a quantitative understanding of hydrogen embrittlement behavior and the knowledge necessary to develop practical design guidelines have not yet been sufficiently established.

Based on these considerations, this study aims to achieve a quantitative understanding of hydrogen embrittlement behavior in martensitic

<sup>\*</sup> Corresponding author.

E-mail address: [kitano.houichi@nims.go.jp](mailto:kitano.houichi@nims.go.jp) (H. Kitano).

<https://doi.org/10.1016/j.matdes.2026.116083>

Received 30 October 2025; Received in revised form 20 April 2026; Accepted 22 April 2026

Available online 23 April 2026

0264-1275/© 2026 The Authors. Published by Elsevier Ltd. This is an open access article under the CC BY license (<http://creativecommons.org/licenses/by/4.0/>).

steels and to construct a mathematical framework applicable to the design of hydrogen embrittlement-resistant martensitic steels. To this end, a data-driven analytical approach was developed and subsequently applied, combining machine learning (ML), SHAP (SHapley Additive exPlanations) analysis [18,19], and symbolic regression.

Specifically, slow strain rate tests (SSRT) were conducted on systematically prepared specimens with varying diffusible hydrogen contents, phosphorus contents, and tempering conditions to construct an experimental database describing the relationship between these parameters and the notch tensile strength, which serves as a representative indicator of hydrogen embrittlement severity. Subsequently, the nonlinear relationships between the influencing factors and the notch tensile strength were modeled using ML. The SHAP analysis was then applied to quantitatively evaluate the contributions of individual factors and their interactions, and the results were simplified and interpreted from physical and metallurgical perspectives, thereby deepening the understanding of hydrogen embrittlement behavior in martensitic steels. Finally, based on the obtained insights, symbolic regression was applied to reconstruct the relationship between the primary factors and the notch tensile strength (i.e., the hydrogen embrittlement state) as an explicit, interpretable equation directly applicable to materials design. The outcomes of this study are expected to provide fundamental knowledge for achieving rational and high-precision design of hydrogen embrittlement-resistant martensitic steels.

## 2. Experimental methods

The material used in this study was equivalent to JIS-SCM440 steel. Five types of steels exhibiting varying phosphorus contents within the JIS standard range ( $< 0.03$  mass%) were utilized. The chemical composition and tensile properties of each steel specimen are listed in Table 1. Steels A, B, and C were produced via vacuum induction melting and casting, whereas steels D and E were commercial steels. The range of.

variations in the factors influencing hydrogen embrittlement, excluding phosphorus content (i.e., diffusible hydrogen content, tempering temperature, and the tempering parameter), are summarized in Table 2. Here, the tempering parameter was defined as  $T(20 + \log t)$  [20,21], where  $T$  and  $t$  denote the tempering temperature and time, respectively, with  $t$  fixed at 5.4 ks. Here,  $\log$  denotes the natural logarithm ( $\ln$ ), and  $T$  is expressed in Kelvin. The logarithmic term is dimensionless; therefore, the tempering parameter is expressed in units of Kelvin.  $T_p$  is linearly proportional to the tempering temperature in this study. The  $T_p$  formulation is introduced for consistency with conventional tempering analysis and to allow potential extension to datasets with variable tempering times.

Each specimen underwent oil quenching after austenitization at 1153 K for 30 min, followed by tempering at the temperatures listed in Table 2 for 5.4 ks, and water cooling. The tensile properties of the steels following tempering are listed in Table 3. Tensile testing was performed at a crosshead speed of  $0.85 \text{ mm min}^{-1}$  utilizing a JIS 14A specimen with a parallel section 6 mm in diameter and 42 mm in length. The dimensions of the notched tensile test specimens used in the SSRT are shown in Fig. 1. Electrochemical hydrogen charging was performed on the notched tensile specimens in 0.1 N NaOH solution or 3%NaCl + 0.3% $\text{NH}_4\text{SCN}$  solution at current densities of  $0.2\text{--}32 \text{ A m}^{-2}$  for 24–168 h

**Table 1**  
Chemical compositions of materials (mass %).

Steels	C	Si	Cr	Mn	Mo	P	S	Fe
A	0.40	0.24	1.04	0.73	0.22	$<0.001$	$<0.001$	Bal.
B	0.41	0.25	1.02	0.69	0.20	0.001	$<0.001$	Bal.
C	0.40	0.24	0.99	0.70	0.20	0.018	$<0.001$	Bal.
D	0.40	0.28	1.08	0.82	0.18	0.015	0.016	Bal.
E	0.40	0.18	1.00	0.76	0.16	0.026	0.010	Bal.

**Table 2**

Parameter ranges for hydrogen embrittlement evaluation.

Parameter	Range
Hydrogen content (ppm)	0–4.68
Tempering temperature (K)	723–903
Tempering parameter	$2.07 \times 10^4\text{--}2.58 \times 10^4$

at ambient temperature. After charging for 24–72 h, Cd plating was applied to prevent hydrogen release, and SSRT was performed at a crosshead speed of  $0.005 \text{ mm min}^{-1}$  on the specimens, following which the Cd coating was removed. However, for specimens charged with hydrogen for 168 h, Cd plating was not applied because a recent study demonstrated that hydrogen release during the SSRT is negligibly small [22]. The unplated specimens were tensioned at a crosshead speed of  $1 \text{ mm min}^{-1}$  to a nominal stress of 230 MPa at the notch to avoid hydrogen release as much as possible, and subjected to SSRT at a crosshead speed of  $0.005 \text{ mm min}^{-1}$ . All specimens were stored in liquid nitrogen until thermal desorption spectrometry (TDS) analysis.

To determine the diffusible hydrogen content, TDS analysis was conducted at a heating rate of  $100 \text{ K h}^{-1}$  via quadrupole mass spectrometry (R-DEC: HTDS-002 and 003). Calibration was performed employing a standard leak hydrogen gas system with a crimper capillary prior to each hydrogen desorption measurement. The diffusible hydrogen content was defined as the cumulative hydrogen content desorbed from the ambient temperature to 573 K, where the first desorption rate peak ended. A total of 69 specimens were prepared within the parameter ranges listed in Table 2. Additionally, for some of the specimens, the microstructures and fracture surfaces were observed via scanning electron microscopy (SEM, JEOL: JSM-7900).

## 3. Data analysis methods

### 3.1. Machine learning model construction

A machine learning model was developed to predict the notch tensile strength  $\sigma_N$  using diffusible hydrogen content  $H_D$ , phosphorus content  $P$ , and tempering parameter  $T_p$  as inputs. These three factors have been identified in previous studies [14–17] as the principal parameters governing hydrogen embrittlement in martensitic steels.

The machine learning model was implemented as a multi-layer perceptron (MLP).

with a neuron architecture of 3 (input)–128 (hidden neurons)–128 (output neurons) – 1.

(output), as shown in Fig. 2. Parametric Rectified Linear Unit (PReLU) function [23] was used as the activation function for the hidden layers and a 5% dropout rate was applied to enhance the generalization performance of the model. The Lion optimizer (learning rate:  $1 \times 10^{-5}$ , weight decay:  $1 \times 10^{-2}$ ) [24] was used for training, and the loss function was defined as the mean log-cosh error with an additional L2 penalty term. Although the MLP provides a flexible nonlinear approximation capability, it is well recognized that for small datasets alternative models, such as Gaussian Process Regression (GPR) or Support Vector Regression (SVR), may achieve competitive or superior predictive performance. Therefore, baseline comparisons using GPR and SVR were conducted under the same cross-validation framework to benchmark the performance of the MLP model. The comparative results are presented in Section 4.2.

Because the available dataset consists of 69 input–output relationships, robustness under limited data conditions was explicitly evaluated. To assess the stability of the learned relationships within the experimentally investigated parameter domain, 5-fold cross-validation was performed. In each fold, model parameters were optimized using a training subset, and predictive performance was evaluated on the remaining fold. To avoid data leakage, normalization parameters were fitted exclusively using the training subset in each fold and subsequently

**Table 3**  
Tensile properties of steels after tempering.

Steels	Tempering Temperature (K)	0.2% proof stress (MPa)	Tensile strength (MPa)	Uniform elongation (%)	Total Elongation (%)	Reduction of area (%)
A	873	856	996	6.4	16.7	68
B	793	1095	1194	5.5	16.4	64
	903	822	942	7.4	20.0	70
C	793	1101	1193	5.0	14.6	60
	903	820	951	7.6	20.7	68
D	723	1338	1439	3.8	11.9	54
	873	916	1043	6.5	17.3	63
E	723	1303	1430	3.7	12.6	58
	873	906	1019	6.8	18.0	67

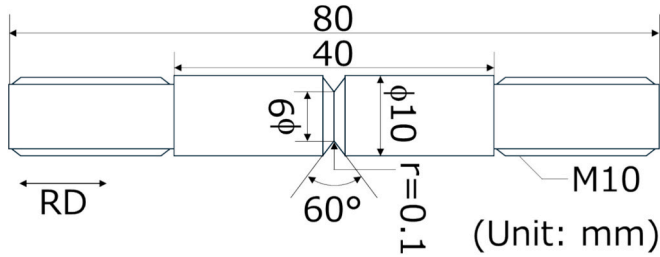


**Fig. 1.** Dimensions of SSRT specimen.

applied to the corresponding validation and test subsets. Stratification was performed such that each fold contained representative samples from the five steels with different phosphorus contents used in this study.

It should be emphasized that the objective of the present study is not to construct a broadly extrapolative predictive model beyond the experimentally explored parameter space. Rather, the purpose is to extract and quantitatively interpret the structure–property relationships within the observed domain defined by the ranges of  $H$ ,  $P$ , and  $T_p$ . Because hydrogen embrittlement behavior is governed by continuous thermodynamic and diffusion-controlled processes, the underlying mapping is expected to be smooth within this domain, which supports interpolation-based modeling.

After confirming robustness via cross-validation, a final model was retrained using the full dataset to maximize information utilization

within the investigated parameter space. Such a procedure—validation via cross-validation followed by retraining on the complete dataset—is a standard practice in statistical learning when constructing a final model for interpretation within a defined domain. This final model was subsequently used for SHAP analysis and symbolic regression.

### 3.2. Shapley additive exPlanations (SHAP)

SHAP is an extension of the Shapley value evaluation method based on cooperative game theory, and is used to quantitatively evaluate the contribution of each input to the output in a machine learning model [19]. In this study, n-Shapley values, a metric proposed to establish the correspondence between SHAP and generalized additive models (GAMs), and to appropriately evaluate interactions, were employed [18]. The n-Shapley values of the final model trained on the full dataset were calculated using the Python library developed by Bordt et al. [25] and the interactions of up to two factors were evaluated. When interactions up to two factors were considered, the notch tensile strength  $\sigma_N$  can be expressed as follows:

$$\sigma_N = (nshap)_{H_D} + (nshap)_P + (nshap)_{T_p} + (nshap)_{H_D \times P} + (nshap)_{P \times T_p} + (nshap)_{T_p \times H_D} + \text{Base value} \quad (1)$$

Here,  $nshap$  represents the n-Shapley value and the subscripts indicate the factors being evaluated. The symbol  $\times$  denotes the interaction between two factors. For instance,  $(nshap)_{H_D}$  represents the contribution of diffusible hydrogen content  $H_D$  to the variation in  $\sigma_N$  (similarly for  $(nshap)_P$ ,  $(nshap)_{T_p}$ ), while  $(nshap)_{H_D \times P}$  represents

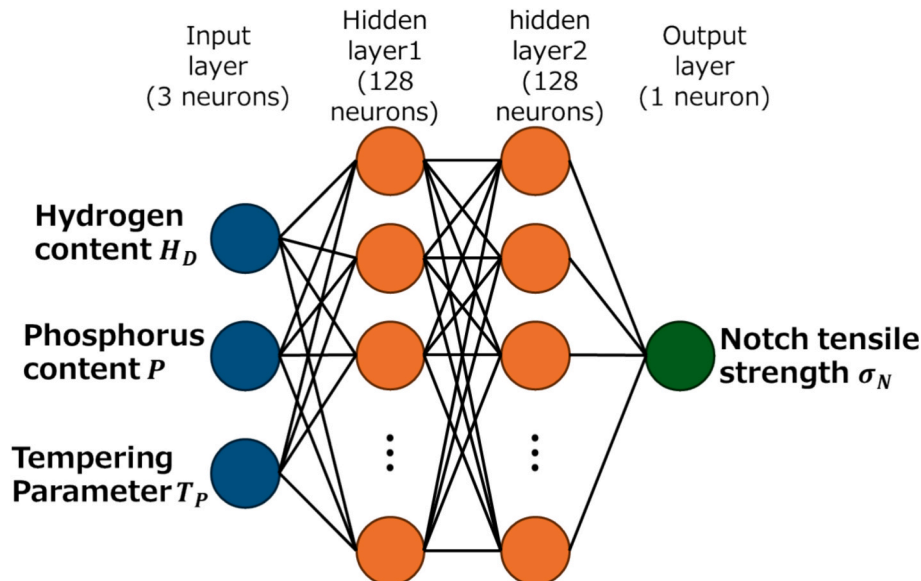


**Fig. 2.** Structure of the multi-layer perceptron model.

the combined influence of  $H_D$  and phosphorus content  $P$  on  $\sigma_N$ . The base value was defined as the predicted notch tensile strength under the experimental condition exhibiting the maximum strength in the dataset. This choice allows direct interpretation of n-Shapley values as contributions to strength reduction from the most resistant state. Using a dataset-average baseline yields qualitatively identical dependency trends, differing only by a constant offset. It should be emphasized that this base value is defined within the present experimental domain and serves as a relative reference rather than an absolute material constant. If the framework is extended to other steels or broader compositional and processing spaces, the base value should be redefined within the corresponding domain to maintain a consistent interpretation of the SHAP contributions.

## 4. Results and discussion

### 4.1. Experimental results

Fig. 3 presents the notch tensile strengths obtained from the SSRT at each tempering temperature. This figure indicates that the trend of decreasing notch tensile strength with increasing diffusible hydrogen content differs between the lower and higher tempering temperatures.

For the two lower tempering temperature conditions (723 K and 793 K), the notch tensile strength was high when the diffusible hydrogen content was less than 1.0 ppm but decreased sharply with increasing diffusible hydrogen content. In contrast, for the two higher tempering temperatures (873 K, 903 K), the notch tensile strength with small diffusible hydrogen content (less than 0.5 ppm) was lower compared with the former two conditions; however, the decrease in the notch tensile strength with increasing diffusible hydrogen content was more

gradual.

Furthermore, as is particularly evident from Fig. 3(a), changes in the phosphorus content at the same tempering temperature tended to affect the notch tensile strength. However, a higher phosphorus content did not necessarily result in a decrease in notch tensile strength, indicating the need for a more detailed evaluation.

### 4.2. Machine learning model construction and SHAP value analysis results

As described in Section 3.1, robustness of the ML model was evaluated via 5-fold cross-validation. Across the five folds, the model achieved a root-mean-square error (RMSE) of  $164.5 \pm 48.4$  MPa and a mean absolute error (MAE) of  $121.4 \pm 32.1$  MPa.

(mean  $\pm$  standard deviation), indicating stable interpolation performance within the experimentally investigated parameter space.

Baseline comparisons using Support Vector Regression (SVR) and Gaussian Process Regression (GPR) were performed under the same cross-validation protocol. The mean RMSE (MPa) across folds was 164.5 for the MLP, 232.8 for SVR (RBF kernel), 214.9 for GPR (RBF kernel), and 161.7 for GPR (Matern 3/2 kernel). These results indicate that the MLP achieves predictive performance comparable to the best-performing GPR model and superior to the other baselines within the investigated domain. Although GPR with a Matern 3/2 kernel exhibited a slightly lower mean RMSE, the MLP was retained as the primary model for subsequent analysis. This choice reflects the objective of the present study, which emphasizes structural interpretation through SHAP decomposition and subsequent symbolic regression rather than purely predictive optimization. The MLP provides a smooth nonlinear mapping that facilitates stable extraction of interaction patterns across the

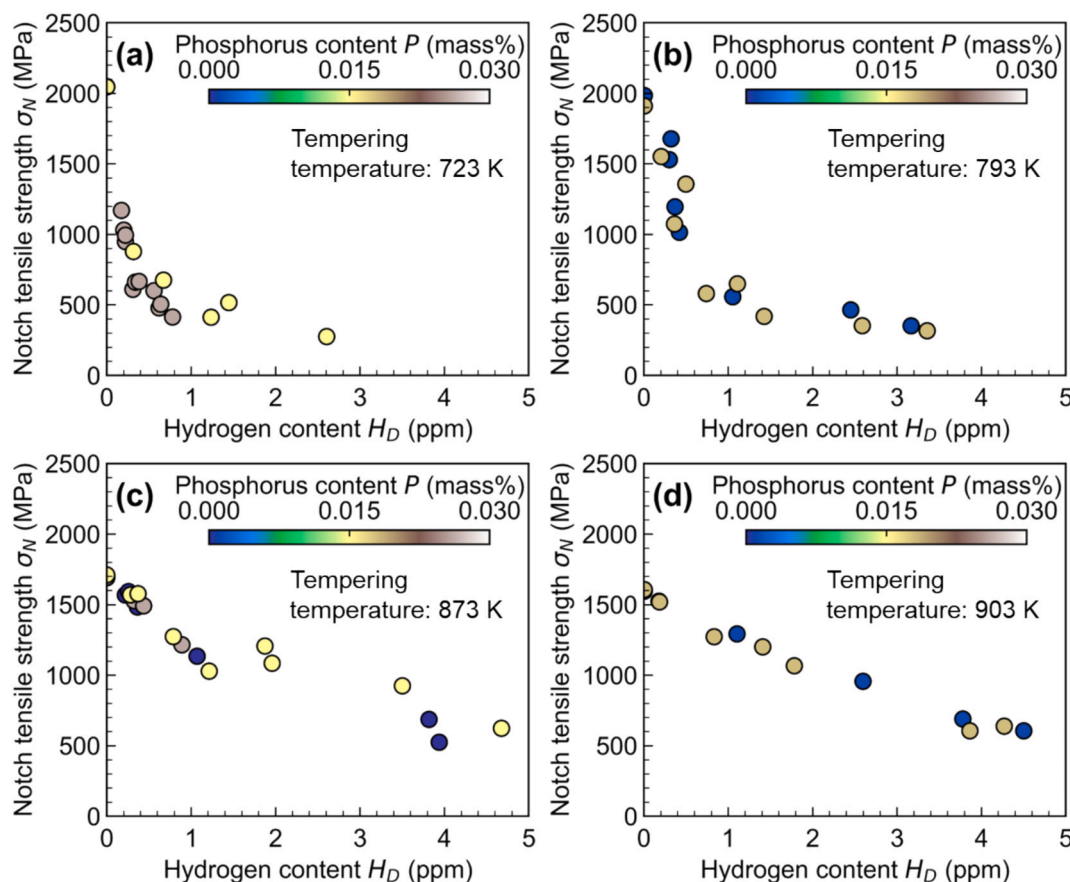


Fig. 3. Notch tensile strength of SSRT specimens tempered at (a) 723 K, (b) 793 K, (c) 873 K, (d) 903 K. 0.1 N NaOH aqueous solution was mainly used for hydrogen charging in the low- $H_D$  range (up to 0.6 ppm), above which 3% NaCl + 0.3%  $\text{NH}_4\text{SCN}$  aqueous solution was used.



investigated parameter space.

After confirming this stability, the model was retrained using the full dataset and used as the final model for subsequent analysis. Fig. 4 compares the predicted notch tensile strength values obtained from the final model with the corresponding experimental results.

As shown in Fig. 4, the predictions are in good agreement with the experimental data across the entire dataset. The model successfully reproduces the characteristic nonlinear dependence of notch tensile strength on diffusible hydrogen content, phosphorus content, and tempering parameter. It should be noted that the present model is intended for structural interpretation within the experimentally explored parameter space rather than extrapolative prediction beyond it.

Fig. 5 presents the n-Shapley values calculated employing the final full-dataset model. The base value was set at 2043 MPa, the output of the final model observed under the experimental condition that exhibited the highest notch tensile strengths specifically, a tempering temperature of 723 K, hydrogen content of 0 ppm, and phosphorus content of 0.015 mass%. These figures provide an overview of the individual factors and the corresponding interactions influencing the notch tensile strength. For example, Fig. 5(a) demonstrates that as the diffusible hydrogen content increases, the n-Shapley value decreases, indicative of a reduction in the notch tensile strength with increasing diffusible hydrogen content. The effects of other factors were also observed. However, the magnitude and variation of each n-Shapley value are complex, and a quantitative understanding based solely on the results presented in Fig. 5 remains challenging. Therefore, in the following section, the SHAP analysis results are simplified and interpreted from a metallurgical viewpoint to elucidate the relationships among the factors.

### 4.3. Simplification of SHAP analysis results and construction of symbolic regression equation

#### 4.3.1. Simplification of SHAP analysis results

To extract meaningful trends from the n-Shapley values shown in Fig. 5, the results were simplified by examining the variation of each factor and interaction term. The factors  $(nshap)_{H_D}$ ,  $(nshap)_P$ ,  $(nshap)_{T_P}$ , shown in Fig. 5(a)–(c), are functions of the diffusible hydrogen content  $H_D$ , phosphorus content  $P$ , and tempering parameter  $T_P$ , respectively.  $(nshap)_{H_D \times P}$ , shown in Fig. 5(d), is a function of  $H_D$  and  $P$ . Although slight variations were observed for small  $H_D$ , the n-Shapley value is nearly constant for most combinations of  $H_D$  and  $P$ . This indicates that the interaction effect of  $H_D$  and  $P$  on  $\sigma_N$  is nearly constant. Therefore, for simplicity,  $(nshap)_{H_D \times P}$  was approximated by its mean value over all samples, denoted as  $(nshap)_{H_D \times P}^{mean}$ . Further, despite the slight variations observed at a  $T_P$  value of approximately 23500, the n-Shapley value was nearly constant for most combinations of  $P$  and  $T_P$ ; hence,  $(nshap)_{P \times T_P}$  was approximated by its mean value, denoted as  $(nshap)_{P \times T_P}^{mean}$ . However,

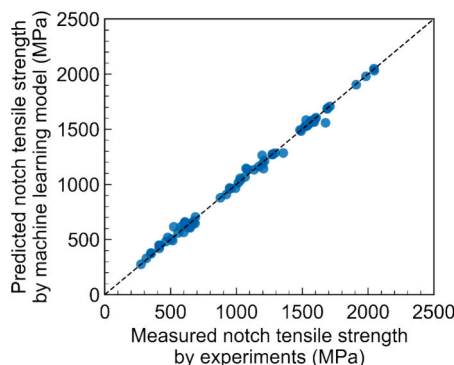


Fig. 4. Comparison of MLP model predictions with experimental results.

$(nshap)_{T_P \times H_D}$  shown in Fig. 5(f) depends on both  $H_D$  and  $T_P$  and is treated as a function of both the variables. Based on these considerations, Eq. (1) can be written as follows:

$$\begin{aligned} \sigma_N &= S_1(H_D, T_P) + S_2(P) + \text{Base value}' S_1(H_D, T_P) \\ &= (nshap)_{H_D} + (nshap)_{T_P} + (nshap)_{T_P \times H_D} S_2(P) = (nshap)_P, \end{aligned} \quad (2)$$

$$\text{Base value}' = \text{Base value} + (nshap)_{H_D \times P}^{mean} + (nshap)_{P \times T_P}^{mean}$$

In this expression,  $S_1(H_D, T_P)$ , represents the combined effects of diffusible hydrogen content and tempering conditions, and  $S_2(P)$  represents the effect of phosphorus content. To verify that this simplification does not significantly distort the original SHAP decomposition, the reconstructed notch tensile strength obtained from the full SHAP formulation was compared with that obtained from Eq. (2). The coefficient of determination between the two reconstructions was  $R^2 = 0.98$ , indicating that the simplified representation preserves nearly all of the variance in  $\sigma_N$  within the investigated parameter space.

The calculated results of  $S_1(H_D, T_P)$  and  $S_2(P)$  are shown in Fig. 6. As a result, Eq. (2) and Fig. 6 provides a simplified representation that captures the dominant contributions and interactions, and is suitable for both metallurgical interpretation and symbolic-regression modeling.

#### 4.3.2. Metallurgical interpretation based on the simplified SHAP analysis

The simplified SHAP results shown in Fig. 6 revealed characteristic dependencies of the notch tensile strength ( $\sigma_N$ ) on the influencing factors. The main findings are summarized as follows:

- Notch tensile strength changes significantly when the tempering temperature is below or above a certain threshold.
- When the diffusible hydrogen content is low, the notched tensile strength decreases sharply. In contrast, when the diffusible hydrogen content is high, it decreases gradually. This tendency is particularly pronounced at lower tempering temperatures.
- Within the composition and experimental ranges investigated in this study, the influence of phosphorus content on notch tensile strength does not exhibit significant.

interaction with diffusible hydrogen content or tempering temperature.

- Notch tensile strength is maximized at a phosphorus content of around 0.01 mass%, with the strength decreasing at both higher and lower phosphorus contents.

The mechanisms underlying these features are discussed below from a metallurgical perspective.

(a) Influence of tempering temperature on notch tensile strength: A comparison of the microstructure observations of specimens tempered at 793 K (low tempering temperature) and 903 K (high tempering temperature), as shown in Fig. 7, reveals that the morphology of the carbides changes significantly with the tempering temperatures. At lower tempering temperatures, carbides exhibit a film-like morphology, visible prominently in the areas highlighted in red in Fig. 7(a) and (b). In contrast, at higher tempering temperatures, the carbides exhibited a granular morphology, as shown in the areas highlighted with blue in Fig. 7(c) and (d). This morphological difference.

significantly affects the accumulation of diffusible hydrogen, which is likely the cause of the large change in notch tensile strength. Similar trend has also been reported by S. G. Kim et al. [15].

(b) Influence of diffusible hydrogen content: This effect is considered to be caused by the transition of the fracture morphology. Fracture surface observations of the specimens with different diffusible hydrogen contents, at tempering temperatures 793 and 903 K and.

0.01 mass% phosphorus content, are shown in Figs. 8 and 9, respectively. From Fig. 8, it can be observed that when the tempering temperature is 793 K, the fracture morphology transitions as the diffusible hydrogen content increases from 0 ppm to 0.3 and 3.17 ppm. Specifically, the surface with a diffusible hydrogen content of 0 ppm

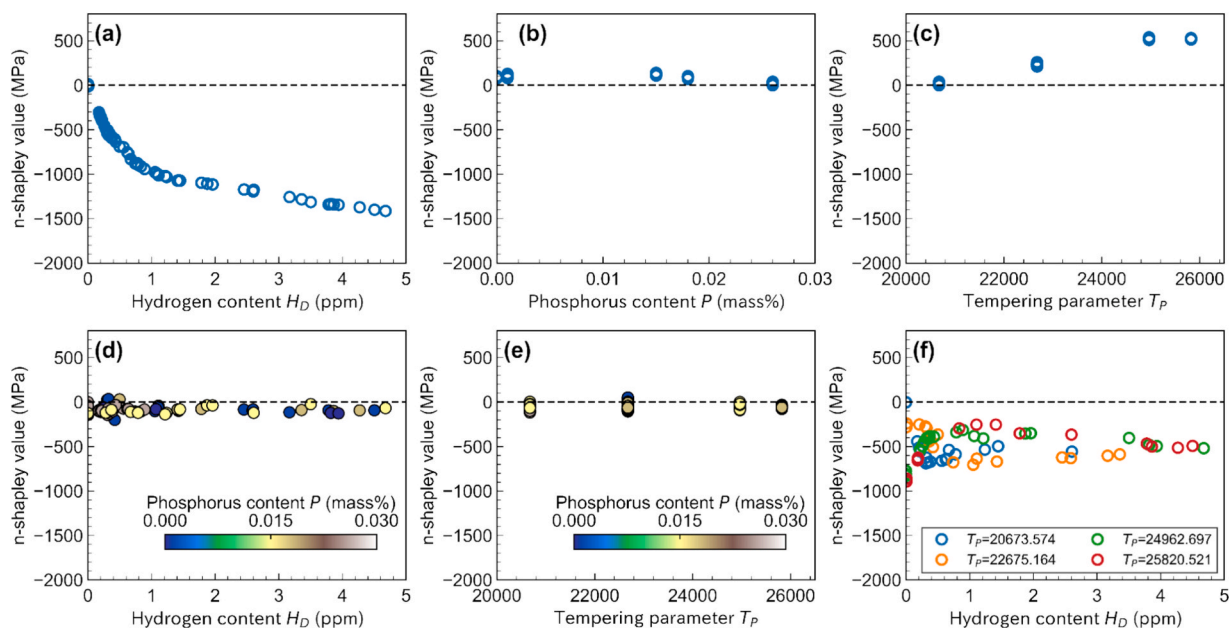


Fig. 5. N-shapley dependency plots for each factor. (a)  $(nshap)_{H_D}$ , (b)  $(nshap)_P$ , (c)  $(nshap)_{T_P}$ , (d)  $(nshap)_{H_D \times P}$ , (e)  $(nshap)_{P \times T_P}$ , (f)  $(nshap)_{T_P \times H_D}$ .

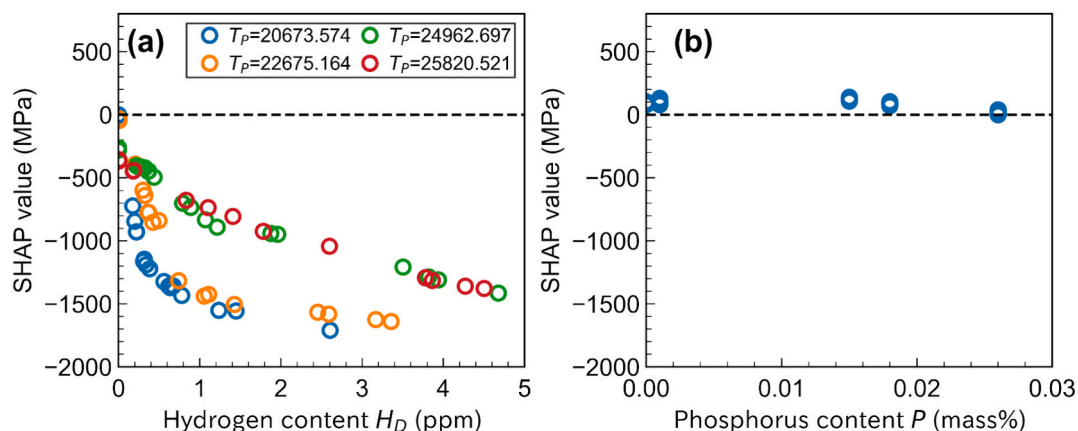


Fig. 6. Simplified n-Shapley values. (a)  $S_1$  and (b)  $S_2$ .

exhibits ductile fracture characteristics with dimples, along with some cleavage facets (Fig. 8(a)). Additionally, the fracture surface at a diffusible hydrogen content of 0.3 ppm primarily exhibits quasi-cleavage features with some intergranular fracture areas (Fig. 8(b)). It has been reported that the intense local plastic work is involved in the propagation of quasi-cleavage fracture [26]. By contrast, at 3.17 ppm, intergranular fracture is predominant (Fig. 8(c)). The predominance of intergranular fracture at higher hydrogen contents is consistent with the notion that hydrogen degrades cohesive strength of prior austenite grain boundaries. On the other hand, at a tempering temperature of 903 K, as shown in Fig. 9, the intergranular fracture was not observed, even at high diffusible hydrogen contents. Furthermore, little change in the fracture morphology with increasing diffusible hydrogen content was observed. This indicates that tempering mitigates susceptibility to hydrogen-assisted decohesion along prior austenite grain boundaries. In this regime, where quasi-cleavage or ductile features remain dominant, the influence of hydrogen can be interpreted primarily in terms of fracture accompanied by intense plastic deformation, without fully suppressing grain-boundary cohesion. These results suggest that the initial rapid decrease in strength with increasing diffusible hydrogen content, particularly pronounced at lower tempering temperatures, corresponds to the transition of the fracture mode from quasi-cleavage

to intergranular fracture. In regions where the dominant fracture mode does not change, the rate of strength reduction owing to the increased diffusible hydrogen content decreases.

(c) Influence of phosphorus content: Phosphorus content was observed to vary only within the narrow range specified by the JIS standard in this study. When a larger amount of phosphorus is present, interactions between the diffusible hydrogen content and tempering temperature were expected to occur. The existence of such interaction terms was suggested by Yamaguchi et al. [27], from a study which utilized first-principles calculations to investigate the effects of impurity elements on hydrogen embrittlement in steel materials.

(d) Notch tensile strength maximized at around 0.01 mass% phosphorus: This behavior can be explained by the interplay of the strengthening and embrittlement effects. As the phosphorus content increases from zero, material strength correspondingly increases owing to the solid-solution strengthening, resulting in an increase in the notch tensile strength. However, as the phosphorus content exceeds approximately 0.01 mass%, the embrittlement effect, the primary reduction of cohesive energy of grain boundaries, outweighs the increase in the strength, thereby resulting in a decrease in notch tensile strength.

Thus, the simplified SHAP analysis provided a deeper metallurgical understanding of the effects and interactions of the main factors ( $H_D$ ,  $P$ ,

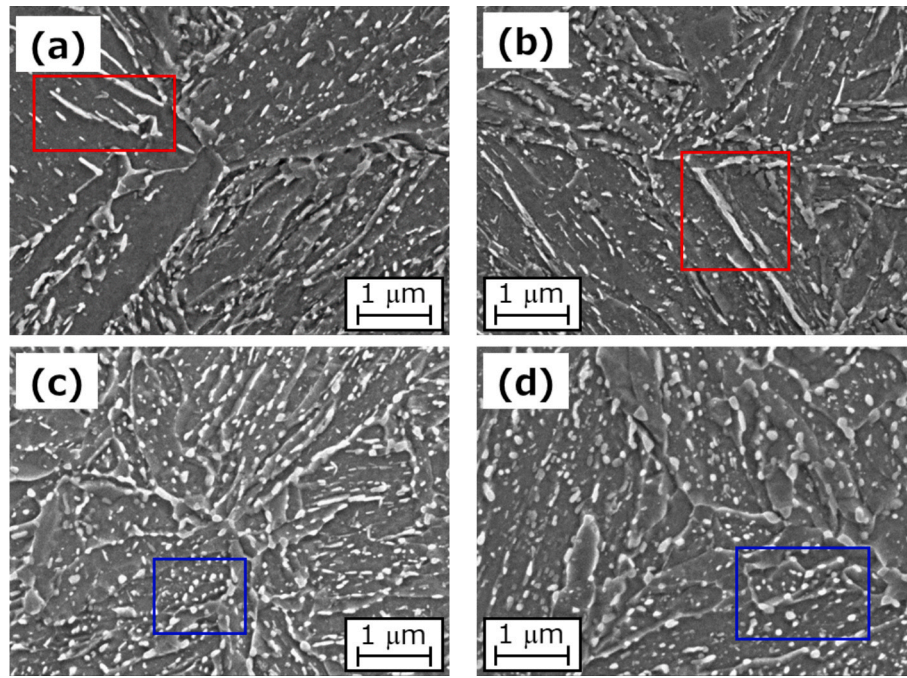


**Fig. 7.** SEM micrographs of JIS-SCM440 steel samples with different tempering temperatures and phosphorus contents (The squares indicate cementite). (a) Tempered at 793 K, phosphorus content 0.001 mass%, (b) Tempered at 793 K, phosphorus content 0.018 mass%, (c) Tempered at 903 K, phosphorus content 0.001 mass%, (d) Tempered at 903 K, phosphorus content 0.018 mass%.

and  $T_p$ ) governing hydrogen embrittlement behavior in martensitic steels. To quantitatively describe this understanding in a form applicable to materials design, the next section develops a symbolic regression model that explicitly expresses these relationships.

#### 4.3.3. Construction and validation of the symbolic regression model

In this section, symbolic regression was performed separately for  $S_1$  and  $S_2$  in Eq. (2). First, for  $S_1(H_D, T_p)$ , the effects of diffusible hydrogen content and tempering conditions were modeled to reproduce the characteristic trends described in (a) and (b) of Section 4.3.2—that is, the significant change in notch tensile strength depending on whether the tempering temperature is below or above a certain threshold, and the sharp decrease in strength at low  $H_D$  followed by a gradual decrease at higher  $H_D$ . To represent this behavior,  $S_1$  was approximated by the following equations, with  $a_1$  to  $l_1$  as unknowns:

$$\begin{aligned} S_1(H_D, T_p) &= A \exp\left(-(BH_D)^2\right) + C \text{sigmoid}(D(H_D + E)) + F, A \\ &= a_1 \text{sgn}(T_p) + b_1, B = c_1 T_p^2 + e_1, C = f_1 \text{sgn}(T_p) + g_1, D \\ &= h_1 \text{sgn}(T_p) + i_1, E = j_1, F = k_1 \text{sgn}(T_p) + l_1, T_p = T_p - d_1 \end{aligned} \quad (3)$$

Here,  $\text{sgn}$  is the sign function and  $\text{sigmoid}(x) = \frac{1}{1+\exp(-x)}$ . The first term represents the sharp decrease in  $S_1$  at low hydrogen contents. As discussed in Section 4.3.2, this rapid reduction is primarily associated with the transition of fracture morphology. However, careful examination of the behavior of  $S_1$  in Fig. 6(a) reveals that even in tempering conditions around  $T_p \approx 24962$  and  $25820$ —where the fracture mode transition is not pronounced—the reduction in  $S_1$  at low hydrogen contents remains larger than that observed at higher hydrogen levels. This suggests that, even when the dominant fracture mode does not change, variations in diffusible hydrogen content may still influence hydrogen trapping behavior and local fracture susceptibility. Furthermore, slight differences are observed even among the lower  $T_p$  conditions and among the higher  $T_p$  conditions. These differences are not necessarily attributable to a drastic transition between film-like and granular carbides, but rather to more subtle variations in carbide morphology and spatial

distribution within each tempering regime. Even within the lower  $T_p$  or higher  $T_p$  conditions, differences in carbide arrangement and associated hydrogen trapping behavior may influence local fracture susceptibility, leading to variations in the magnitude of  $S_1$ . Taking these considerations into account, the first term was formulated using a coefficient  $A$  that differs between lower and higher  $T_p$  conditions, combined with a Gaussian-type function to represent the rapid hydrogen-induced decrease. The quadratic dependence on  $T_p$  included in the internal parameter  $B$  provides a compact representation of tempering-dependent hydrogen sensitivity. However, this quadratic form should not be regarded as definitive. It represents a minimal parametric approximation of the observed tempering dependence within the present dataset. A more detailed mechanistic understanding of the tempering effect on hydrogen sensitivity would require experimental data with more finely varied tempering conditions, which constitutes an important direction for future work.

The second term represents the gradual reduction in  $S_1$  at higher hydrogen contents. Unlike the Gaussian term, which captures the abrupt strength drop associated with fracture mode transition, this sigmoidal component describes the continued degradation

in regions where the dominant fracture mode does not change. The coefficients associated with  $\text{sgn}(T_p)$  allow the magnitude and rate of this gradual degradation to differ between lower and higher tempering regimes, reflecting the experimentally observed differences in fracture sensitivity and hydrogen trapping characteristics.

Next, for  $S_2(P)$ , the effect of phosphorus content was modeled to reproduce the characteristic behaviors discussed in (c) and (d) of Section 4.3.2—namely, that within the investigated composition range, the influence of phosphorus on notch tensile strength does not show significant interaction with diffusible hydrogen content or tempering temperature, and that the strength exhibits a maximum at around 0.01 mass% phosphorus, decreasing at both higher and lower concentrations. To represent this behavior,  $S_2$  was approximated by the following equations, with  $a_2$ ,  $b_2$ , and  $c_2$  as unknowns:

$$S_2(P) = a_2(P - b_2)^2 + c_2 \quad (4)$$



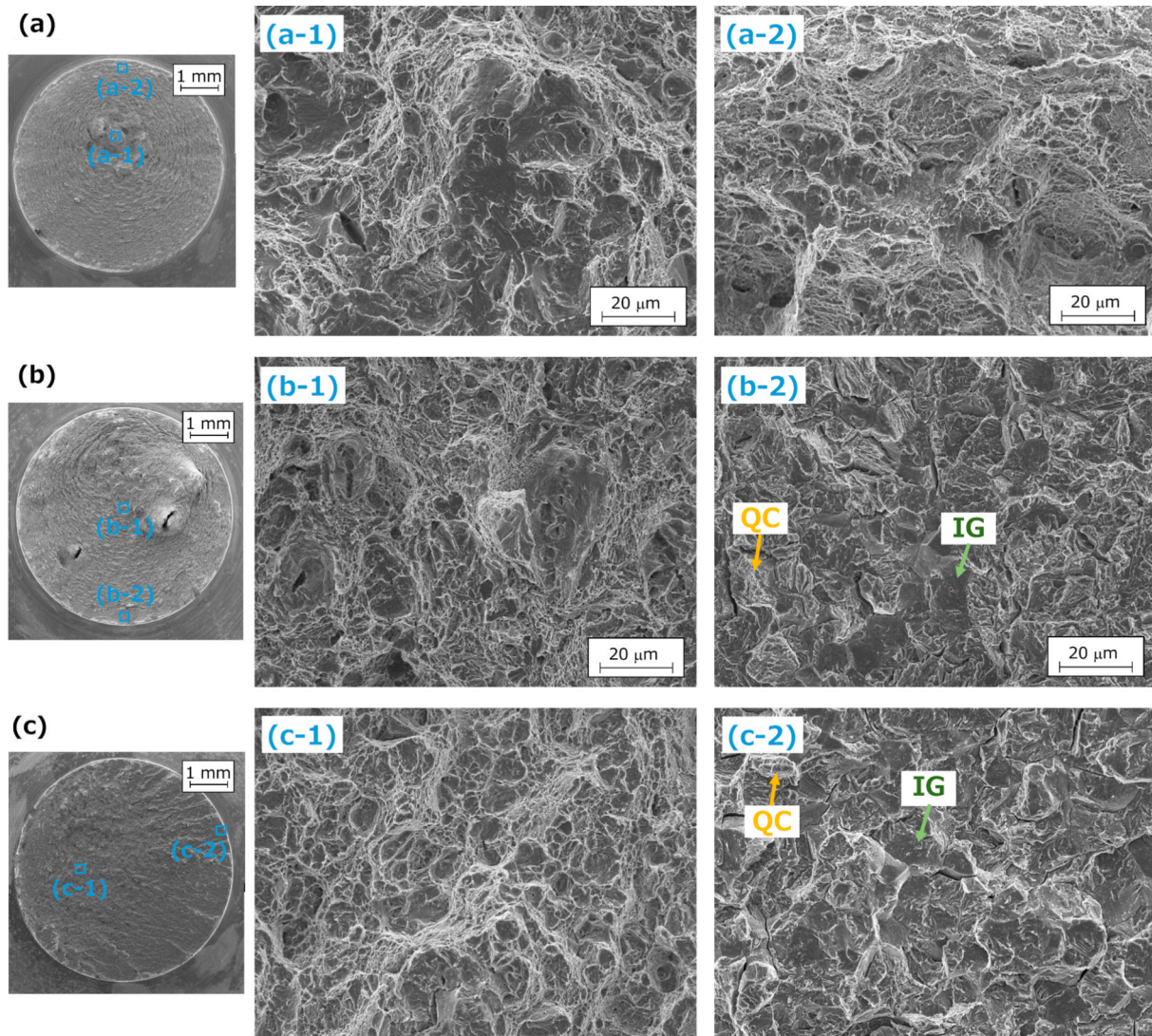


**Fig. 8.** Fracture surface morphologies of samples tempered at 793 K with 0.001 mass% phosphorus content, showing the effect of different diffusible hydrogen contents. The figures on the left are the entire fracture surface, and the other figures are enlarged views. (a) Diffusible hydrogen content: 0 ppm, (b) Diffusible hydrogen content: 0.30 ppm, (c) Diffusible hydrogen content: 3.17 ppm. The regions labeled “QC” and “IG” indicate quasi-cleavage facets and intergranular fracture regions, respectively. In Fig. 8(b)-2 and (c)-2, these labels are added to highlight the coexistence and transition between fracture modes.

The quadratic form reflects the competing effects of solid-solution strengthening and grain-boundary embrittlement, leading naturally to a maximum strength at an intermediate phosphorus level.

To determine the unknown coefficients in Eqs. (3) and (4), two approaches can be considered: one based on the calculated  $S_1$  and  $S_2$  results shown in Fig. 6, and the other based on the experimental results obtained from the SSRT. In this study, the latter approach was adopted to derive symbolic regression equations that directly represent the experimental relationships. During this process, the constant terms—Base value' in Eq. (2),  $l_1$  in Eq. (3), and  $c_2$  in Eq. (4)—were analyzed collectively. The unknown parameters were determined by the least-squares approximation using the SSRT data, and the obtained results are summarized in Table 4.

The predicted notch tensile strength values calculated from Eqs. (2)–(4) using the coefficients in Table 4 are compared with the SSRT results in Fig. 10. For reference, the symbolic regression equations for each tempering condition, corresponding to Fig. 10(a)–(d), are shown at the bottom of Fig. 10 with the numerical coefficients and constants indicated. The coefficients were slightly simplified for clarity.

As shown in Fig. 10, the predictions obtained from the symbolic regression model are in excellent agreement with the experimental

results, demonstrating that the model accurately reproduces the effects of diffusible hydrogen, phosphorus, and tempering conditions on the notch tensile strength. The residuals between the symbolic regression predictions and the experimental results exhibit a mean error of  $-0.003$  MPa and a standard deviation of 93.9 MPa. The negligible mean error indicates the absence of systematic bias, while the standard deviation provides a quantitative estimate of predictive uncertainty within the investigated parameter domain. The functional structure of Eqs. (3) and (4) reflects the characteristic physical behavior associated with hydrogen embrittlement, enabling a compact yet interpretable representation of the combined effects of the key factors. It should be noted that the regression coefficients themselves are not interpreted as fundamental physical constants; rather, they serve as fitting parameters within a physically motivated functional framework identified through SHAP analysis and experimental observations. This framework bridges data-driven analysis and metallurgical understanding, providing a practical tool for the rational design and safety assessment of hydrogen embrittlement-resistant high-strength steels.



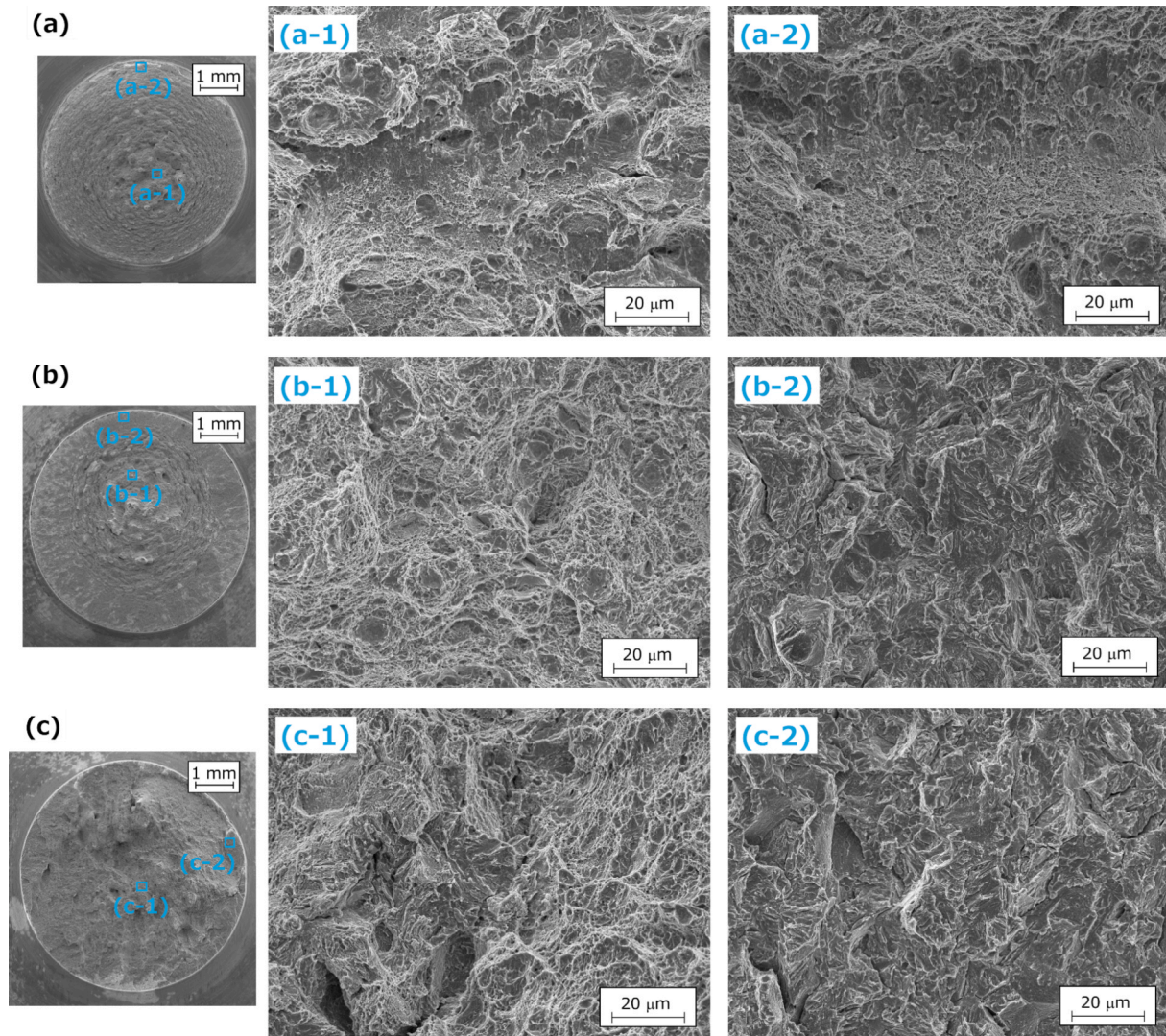


**Fig. 9.** Fracture surface morphologies of samples tempered at 903 K with 0.001 mass% phosphorus content, showing the effect of different diffusible hydrogen contents. The figures on the left are the entire fracture surface, and the other figures are enlarged views. (a) Diffusible hydrogen content: 0 ppm, (b) Diffusible hydrogen content: 2.60 ppm, (c) Diffusible hydrogen content: 3.78 ppm.

**Table 4**  
Determination of unknowns in Eqs. (3) and (4).

Symbol	Value	Symbol	Value
$a_1$	$-4.40 \times 10^2$	$h_1$	-0.76
$b_1$	$8.84 \times 10^2$	$i_1$	-0.68
$c_1$	$2.85 \times 10^7$	$j_1$	-3.06
$d_1$	$2.42 \times 10^4$	$k_1$	$1.29 \times 10^3$
$e_1$	1.49	Base value' + $l_1 + c_2$	$1.82 \times 10^3$
$f_1$	$3.13 \times 10^3$	$a_2$	$-2.08 \times 10^5$
$g_1$	$-2.42 \times 10^3$	$b_2$	0.01

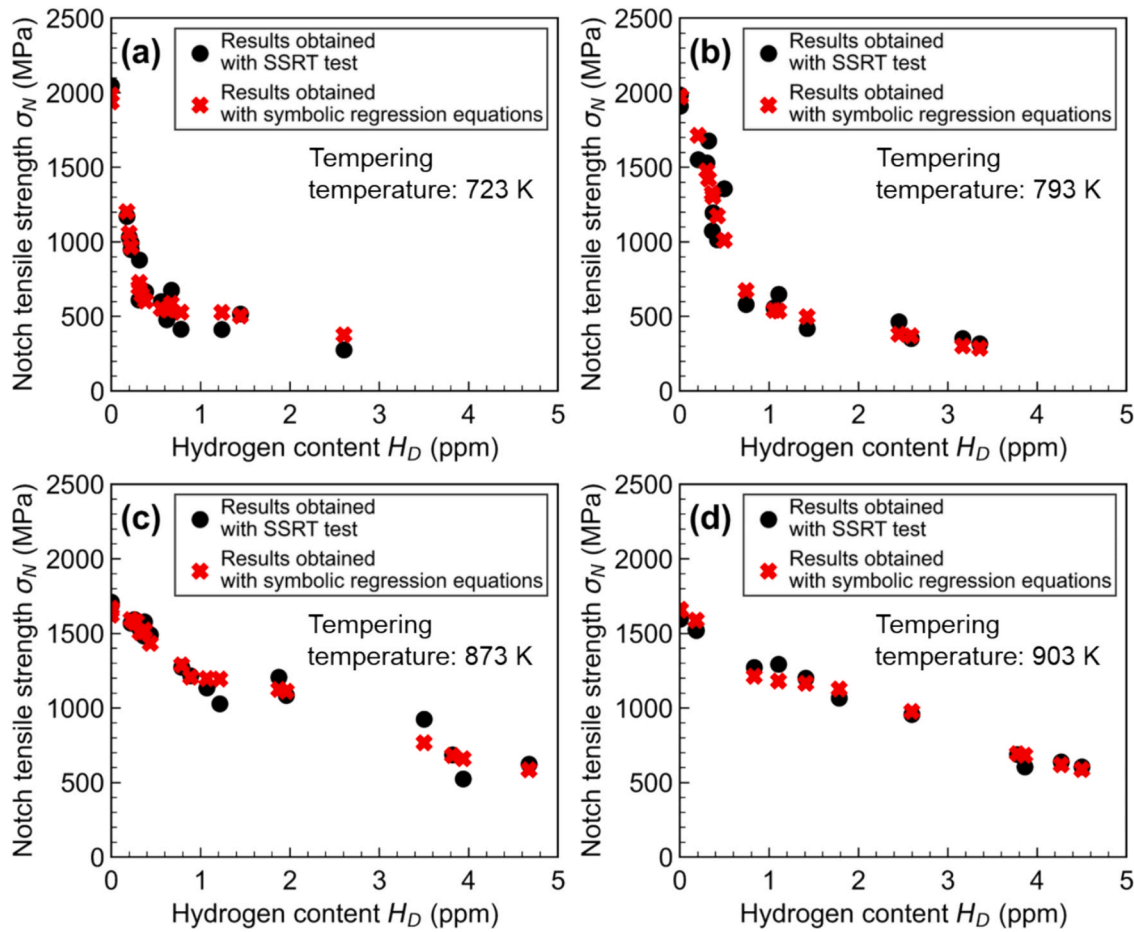
## 5. Conclusions

In this study, a data-driven analytical framework combining machine learning, SHAP analysis, and symbolic regression was developed to achieve a quantitative understanding of hydrogen embrittlement behavior in martensitic steels. The main conclusions are summarized as follows:

1. A machine learning model was successfully constructed to predict the notch tensile strength using diffusible hydrogen content, phosphorus content, and tempering parameter as inputs.

2. SHAP analysis quantitatively evaluated the contributions and interactions of these factors, and the simplified SHAP results clarified the characteristic dependencies of notch tensile strength on each factor and interpreted these dependencies from a metallurgical perspective.
3. Symbolic regression reconstructed these relationships as explicit and interpretable equations that captured the characteristic physical behavior associated with hydrogen embrittlement, quantitatively representing the combined effects of diffusible hydrogen, phosphorus, and tempering conditions.
4. The developed model provides a rational and physically interpretable framework that links data-driven analysis and metallurgical understanding, offering a practical tool for the design and safety assessment of hydrogen embrittlement-resistant high-strength steels.

Notable results include the following: the rapid decrease in notch tensile strength at low diffusible hydrogen contents can be described by a Gaussian function, whereas the gradual decrease at high diffusible hydrogen contents can be represented by a sigmoidal function. The change in notch tensile strength associated with tempering temperature depends strongly on the carbide morphology. Within the composition



#### -Symbolic regression equations for each tempering temperature-

$$\begin{aligned}
 \text{(a)} \quad \sigma_N &= 1325 \exp(-25.6H_D^2) - \frac{5557}{1+\exp(0.24-0.08H_D)} - 208000(P-0.01)^2 + 3111 \\
 \text{(b)} \quad \sigma_N &= 1325 \exp(-4.7H_D^2) - \frac{5557}{1+\exp(0.24-0.08H_D)} - 208000(P-0.01)^2 + 3111 \\
 \text{(c)} \quad \sigma_N &= 444 \exp(-2.7H_D^2) + \frac{711}{1+\exp(-4.4+1.44H_D)} - 208000(P-0.01)^2 + 527 \\
 \text{(d)} \quad \sigma_N &= 444 \exp(-5.0H_D^2) + \frac{711}{1+\exp(-4.4+1.44H_D)} - 208000(P-0.01)^2 + 527
 \end{aligned}$$

**Fig. 10.** Comparison of symbolic regression predictions and experimental results for SSRT specimens tempered at (a) 723 K, (b) 793 K, (c) 873 K, and (d) 903 K and –Symbolic regression equations for each tempering temperature.

and experimental ranges investigated in this study, the interaction effects of phosphorus with diffusible hydrogen content and tempering condition were not significant compared with the dominant contributions of hydrogen and tempering parameter. These findings reinforce existing metallurgical knowledge while providing new quantitative insights that are highly valuable for the design and safety assessment of hydrogen infrastructure components utilizing high-strength martensitic steels.

While this study focused solely on phosphorus as an impurity element within a limited set of martensitic steels, the quantitative evaluation of additional impurity elements (e.g., S, O), alloying elements, and a broader range of steel grades remains an important subject for future investigation. Furthermore, extending this framework to incorporate environmental variables such as stress state and service conditions will enhance its generalization capability and robustness assessment, contributing to the comprehensive design and reliable deployment of advanced steels for hydrogen infrastructure applications.

#### CRediT authorship contribution statement

**Houichi Kitano:** Writing – original draft, Visualization, Validation, Methodology, Investigation, Formal analysis, Data curation, Conceptualization. **Yuuji Kimura:** Writing – review & editing, Methodology, Data curation, Conceptualization. **Akinobu Shibata:** Writing – review & editing, Supervision, Project administration, Funding acquisition, Conceptualization.

#### Funding

This research was partially supported by the MEXT Program Data Creation and Utilization Type Material Research and Development Project [grant number JPMXP1122684766].

#### Declaration of competing interest

The authors declare that they have no known competing financial

interests or personal relationships that could have appeared to influence the work reported in this paper.

## Acknowledgments

This work was supported by the MEXT Program Data Creation and Utilization Type Material Research and Development Project (grant number JPMXP1122684766).

## Data availability

Data will be made available on request.

## References

- [1] W.W. Gerberich, Y.T. Chen, Hydrogen-controlled cracking—an approach to threshold stress intensity, *Metall. Trans. A* 6 (2) (1975) 271–278.
- [2] R.A. Oriani, P.H. Josephic, Equilibrium aspects of hydrogen-induced cracking of steels, *Acta Metall.* 22 (9) (1974) 1065–1074.
- [3] R.A. Oriani, P.H. Josephic, Equilibrium and kinetic studies of the hydrogen-assisted cracking of steel, *Acta Metall.* 25 (9) (1977) 979–988.
- [4] A.A. Guzmán, R. Janisch, Effects of mechanical stress, chemical potential, and coverage on hydrogen solubility during hydrogen-enhanced decohesion of ferritic steel grain boundaries: a first-principles study, *Phys. Rev. Materials* 8 (2024) 073601.
- [5] M. Yamaguchi, K. Ebihara, M. Itakura, T. Tsuru, Quantitative estimation method of the effect of segregated solute on hydrogen-enhanced decohesion at a grain boundary, *Scr. Mater.* 255 (2025) 116366.
- [6] C.D. Beachem, A new model for hydrogen-assisted cracking (hydrogen “embrittlement”), *Metall. Mater. Trans. B* 3 (1972) 441–455.
- [7] H.K. Birnbaum, P. Sofronis, Hydrogen-enhanced localized plasticity—a mechanism for hydrogen-related fracture, *Mater. Sci. Eng. A* 176 (1) (1994) 191–202.
- [8] P.J. Ferreira, I.M. Robertson, H.K. Birnbaum, Hydrogen effects on the interaction between dislocations, *Acta Mater.* 46 (5) (1998) 1749–1757.
- [9] S. Lynch, Hydrogen embrittlement phenomena and mechanisms, *Corros. Rev.* 30 (3–4) (2012) 105–123.
- [10] I.M. Robertson, The effect of hydrogen on dislocation dynamics, *Eng. Fract. Mech.* 64 (5) (1999) 649–673.
- [11] D. Guedes, L. Cupertino Malheiros, A. Oudriss, S. Cohendoz, J. Bouhattate, J. Creus, F. Thébault, M. Piette, X. Feaugas, The role of plasticity and hydrogen flux in the fracture of a tempered martensitic steel: a new design of mechanical test until fracture to separate the influence of mobile from deeply trapped hydrogen, *Acta Mater.* 186 (2020) 133–148.
- [12] M. Nagumo, Function of Hydrogen in Embrittlement of High-strength Steels, *ISIJ Int.* 41 (6) (2001) 590–598.
- [13] M. Nagumo, H. Matsuda, Function of hydrogen in intergranular fracture of martensitic steels, *Philosophical Magazine A: Physics of Condensed Matter, Structure, Defects and Mechanical Properties* 82 (17–18) (2002) 3415–3425.
- [14] F. Dong, J. Venezuela, H. Li, Z. Shi, Q. Zhou, L. Chen, J. Chen, L. Du, A. Atrains, The influence of phosphorus on the temper embrittlement and hydrogen embrittlement of some dual-phase steels, *Mater. Sci. Eng. A* 854 (2022) 143379.
- [15] S.-G. Kim, J.-Y. Kim, B. Hwang, Effect of Tempering Temperature on Hydrogen Embrittlement of SCM440 Tempered Martensitic Steel, *Materials* (2023).
- [16] B.D. Craig, The effect of Phosphorus Content on the Hydrogen stress Cracking of High Strength 4130 Steel, *Metall. Trans. A* 13 (5) (1982) 907–912.
- [17] S.-I. Komazaki, S. Watanabe, T. Misawa, Influence of Phosphorus and Boron on Hydrogen Embrittlement Susceptibility of High Strength Low Alloy Steel, *ISIJ Int.* 43 (11) (2003) 1851–1857.
- [18] S. Bordt U.v. Luxburg, From Shapley Values to Generalized Additive Models and back R. Francisco D. Jennifer . M. Jan-Willem van de, *Proceedings of the 26th International Conference on Artificial Intelligence and Statistics, PMLR, Proceedings of Machine Learning Research* 2023 709 745.
- [19] S.M. Lundberg, S.-I. Lee, A unified approach to interpreting model predictions, *Proceedings of the 31st International Conference on Neural Information Processing Systems, Curran Associates Inc., Long Beach, California, USA, 2017*, pp. 4768–4777.
- [20] J.H. Hollomon, Time-temperature relations in tempering steel, *Trans. AIM* 162 (1945) 223–249.
- [21] S. Uranaka, M. Takanashi, T. Maeda, T. Masumura, T. Tsuchiyama, Y. Kawamoto, H. Shirahata, Y. Kobayashi, R. Uemori, Effects of Retained Austenite upon Softening during Low-temperature Tempering in Martensitic Carbon Steels, *ISIJ Int.* 64 (2) (2024) 449–458.
- [22] Y. Kimura, T. Moronaga, K. Tsuzaki, Enhanced Resistance to delayed Fracture in 0.09 mass% P-Doped High-Strength Steel Processed by Warm Tempforming, *ISIJ Int.* 65 (1) (2025) 20–25.
- [23] K. He, X. Zhang, S. Ren, J. Sun, Delving deep into Rectifiers: Surpassing Human-Level Performance on ImageNet Classification, *IEEE International Conference on Computer Vision (ICCV) 2015* (2015) 1026–1034.
- [24] X. Chen, C. Liang, D. Huang, E. Real, K. Wang, H. Pham, X. Dong, T. Luong, C.-J. Hsieh, Y. Lu, Q.-V. Le, in: *Symbolic Discovery of Optimization Algorithms*, Curran Associates Inc., New Orleans, LA, USA, 2023, p. 2140.
- [25] nshap. <https://github.com/tml-tuebingen/nshap>.
- [26] A. Shibata, I. Gutierrez-Urrutia, A. Nakamura, T. Moronaga, K. Okada, Y. Madi, J. Besson, T. Hara, Local crack arrestability and deformation microstructure evolution of hydrogen-related fracture in martensitic steel, *Corros. Sci.* 233 (2024) 112092.
- [27] M. Yamaguchi, K. Ebihara, M. Itakura, Multiscale thermodynamic analysis on hydrogen-induced intergranular cracking in an alloy steel with segregated solutes, *Corros. Rev.* 33 (6) (2015) 547–557.